PAPER

The interpretation of magnetic activity associated with pellet injections into plasmas created in the stellarator TJ-II

IOP Publishing | International Atomic Energy Agency Nuclear Fusion

Nucl. Fusion **61** (2021) 076014 (16pp) https://doi.org/10.1088/1741-4326/ac04f6

The interpretation of magnetic activity associated with pellet injections into plasmas created in the stellarator TJ-II

K.J. McCarthy[1,*], E. Ascasíbar[1], N. Tamura[2], N. Panadero[1], I. García-Cortes[1], B. van Milligen[1], A. Cappa[1], R. García[1], J. Hernández-Sánchez[1], M. Liniers[1], G. Motojima[2], M. Navarro[1], I. Pastor[1] and TJ-II Team[1]

[1] Laboratorio Nacional de Fusión, CIEMAT, Madrid, Spain
[2] National Institute for Fusion Science, Toki, Japan

E-mail: kieran.mccarthy@ciemat.es

Received 26 March 2021, revised 21 May 2021
Accepted for publication 25 May 2021
Published 17 June 2021

Abstract

Pellet injection into magnetic confinement plasma is widely employed for plasma fuelling and impurity transport studies. While post-injection effects include changes in density and temperature, several short-lived effects have been identified during and immediately after pellet ablation, e.g. pre-cooling of the plasma core or a strong reduction in fluctuations. Here, transitory effects observed in magnetic signals during and immediately after the injection of fuel and tracer encapsulated solid pellets into microwave and neutral beam heated plasma in the stellarator TJ-II are reported. One effect is the excitation of a clear, short-lived, magnetic instability during the ablation phase of a cryogenic pellet. Another effect is a brief reduction in broadband magnetic fluctuations immediately after an injection while a third effect is frequency jumps of already excited Alfvén eigenmodes (AE) when neutral beam heating is employed. The interpretation of these effects is facilitated by signals from 2 recently installed toroidal arrays of magnetic coils that follow the helicity of this device along one of its quadrants. It is concluded that interactions between outward drifting pellet particles and a low-order rational surface lead to the magnetic instability, that pellet-induced plasma cooling induces a transitory reduction in broadband magnetic fluctuations and that plasma mass density changes dominate jumps in AE frequencies.

Keywords: stellarator, fuel pellet, magnetics, rational surfaces, fluctuations

(Some figures may appear in colour only in the online journal)

1. Introduction

Pellet injection is widely used in magnetic confinement plasma devices for core fuelling, for studying impurity transport, as well as for other objectives [1–3]. While much of the physics of pellet ablation and of the subsequent pellet particle deposition, transport processes and plasma evolution is understood, significant research is still needed to achieve a complete comprehension. The injection of a pellet into hot plasma generates a brief emission of electromagnetic radiation (e.g. Balmer Hα light) and results in transitory changes to plasma parameters such as electron and ion densities and temperatures, stored energy, etc [4]. It is also known to modify plasma turbulence [5]. In addition, several transitory effects have been observed as a pellet travels through the plasma. These effects are observed in different devices and much of the underlying physics has been understood. For instance, effects include a cold wave preceding the pellet [6], cloud detachment from the

* Author to whom any correspondence should be addressed.

pellet producing striations in ablation light profiles [7], fast-electrons incident on a pellet causing increased ablation or pellet rupture [4, 8, 9], and acceleration of a pellet by fast-ion impacts or by cloud pressure asymmetry [10, 11]. Nonetheless, a full understanding of other transitory effects that have been observed remaining outstanding. For instance, short-lived activity in magnetic pick-up coil signals has been reported to accompany pellet ablation in several devices [12–18]. However, to the authors' knowledge, such short-lived activity still needs to be investigated in depth. In contrast, in cases in which energetic-particle driven Alfvén eigenmodes (AEs) are detected using such coils, significant drops are observed in AE frequencies when a pellet is injected, this being primarily associated with the increase in plasma mass density [19, 20]. Additionally, post-injection reductions in magnetic fluctuations have been considered in other devices. For instance, it was reported that signals from Mirnov coils were hardly affected by pellets injected into TFR discharges [21] whereas it was reported that pellet injections into the reversed-field pinch device MST generally resulted in a modest reduction in magnetic fluctuations [22]. In this paper, the authors report on magnetic activity during and immediately after pellet injection into the stellarator TJ-II and attempt to identify the origins of such activity. For this, two different types of pellets, solid hydrogen and tracer-loaded polystyrene ones, are injected into the same TJ-II sector [23] and into both microwave and neutral-beam heated plasmas.

As noted above, bursts of magnetic activity during, or immediately after, pellet ablation have been reported for a number of magnetic confinement devices. For instance, in the Heliotron E device, a burst in poloidal magnetic activity, having a delay of 50 to 100 μs with respect to pellet plasma penetration, was observed with Mirnov coils during the ablation phase [12, 13]. The activity lasted for several 100 μs and was damped as a new density profile was established. A fast Fourier transform (FFT) analysis identified several coherent peaks while a cross-coherence analysis found that parts of these magnetic fluctuations consisted of coherent waves with low toroidal mode numbers corresponding to rational surfaces. Since n/m values were always less than the edge $\iota/2\pi$, it was considered that such coherent modes were associated with corresponding rational surfaces and that the transient behaviour was related to a rapid equilibrium process on the rational surface. Further investigation suggested that these fluctuations could be attributed to a resonant interaction between an incident heat flux on a partially ionized pellet cloud and a rational surface. In a different work involving the injection of sub-millimetre lithium pellets into neutral beam heated plasmas of the tokamak DIII-D, strong fluctuations in the magnetic signal were detected during granule ablation inside the plasma edge [14]. However, to the authors' knowledge these fluctuations were not investigated further. In work on the tokamak JIPP T-IIU, it was reported that, for on-axis and upward off-axis pellet injections during ohmic heating phases, both the ablation cloud and the magnetic fluctuations propagated poloidally in the electron diamagnetic direction [15]. Also, in the FTU device, strong high-frequency magnetic fluctuations (up to 500 kHz) were seen to develop during pellet ablation for high-field side injections [16]. Preliminary results indicated that the observed fluctuations were Alfvén waves generated by drifting plasmoids. More recently, in the tokamak ASDEX Upgrade, coherent pellet-driven oscillations with a toroidal mode number $n = -6$ were detected in the range 100 to 300 kHz [17]. It was reported that the magnetic perturbation strength showed monotonic increase with pellet penetration depth and exponential decay after pellet burnout. An investigation determined that such a pellet-driven magnetic perturbation could not act as the trigger for type-I edge localized modes (ELMs) as the structure of such pellet-driven modes was completely different from pre-ELM observed modes. Next, in the stellarator W7-X, in-vessel Mirnov coils have picked up short strong bursts of magnetic fluctuations, which are spread over a broad range of frequencies, during individual pellet injections along a long series of pellet injections into electron cyclotron resonance heated (ECRH) discharges [18]. Moreover, during such a pellet injection phase, which lasts for about 1 s, it is reported that the overall magnetic fluctuation amplitude reduces slightly. However, a more detailed analysis of these short and strong bursts has not yet been made. Finally, frequency perturbations were observed in magnetic spectrographs during pellet injections into the JET device [19, 20]. In spectrographs showing well-developed fast-ion excited toroidal Alfvén eigenmodes (TAEs) prior to pellet injection, it became impossible to identify their toroidal mode numbers for several milliseconds (3 to 8 ms) after an injection. Moreover, significant jumps in TAE frequencies were observed during a longer post-injection period when such numbers could be determined again, these changes being associated with changes in plasma ion density. Similar perturbations were seen for elliptical AEs. Now, returning to the short periods when toroidal modes numbers were indeterminable, it was noted that these times corresponded to pellet times-of-flight and thus it was considered that the observed broadband magnetic perturbations might be associated with magnetic recombination that occurs during pellet ablation and cloud ionization [24].

In this work, we report on magnetic activity during and immediately after the ablation of pellets injected into ECRH and neutral beam injection (NBI) heated plasmas in the stellarator TJ-II. In many instances, a short burst of strengthened magnetic activity is observed during, and for a short period after, the pellet ablation phase whilst in other instances no such activity is detected. Moreover, broadband magnetic fluctuation levels reduce for a short time period after a pellet injection, this reduction being larger for ECRH plasmas. In addition, frequency jumps in AEs are seen in NBI-heated plasmas in which such modes exist prior to injection. The work reported here has been facilitated by the recent installation on TJ-II of two arrays containing a total of 192 magnetic pick-up coils that follow the helical rotation of this device along one of its quadrants. Finally, in order to highlight these observations, representative examples are presented. Then, using magnetic array signals and measurements from other plasma diagnostics, plus pellet injection simulations, the sources of such activities are investigated.

2. Experimental arrangement

This work was performed on the stellarator TJ-II. It is a Heliac-type stellarator with major radius, R, of 1.5 m that was designed to explore a wide range of rotational transforms, ($0.9 \leqslant \iota_0/2\pi \leqslant 2.2$), in low, negative shear configurations ($\Delta\iota/\iota < 6\%$), where i_0 is the central iota value [25]. Here, $\iota/2\pi = n/m$, where n and m are the toroidal and poloidal helical winding numbers, respectively. In a current-free stellarator, the currents in its external field coils impose the magnetic configuration. In TJ-II, these are the circular, helical, vertical and toroidal field coils and the currents in the first three of these coils are encoded in the configuration label 'xxx_yy_zz'. At low plasma pressures and internal currents, the magnetic configuration and the rotational transform profile are essentially specified by these external currents. This results in a bean-shaped poloidal crosscut of its closed magnetic flux surfaces and an on-axis magnetic field, B_0, that is $\leqslant$1.1 T, an average plasma minor radius, a, that is $\leqslant$0.22 m, and a volume, V_{plasma}, contained within the last-closed magnetic surface that is $\leqslant 1.1\ \text{m}^3$. Plasmas are created using ECRH generated by two gyrotrons operated at 53.2 GHz, i.e. the 2nd harmonic of its electron cyclotron resonance frequency ($P_{\text{ECRH}} \leqslant 500$ kW). With ECRH, plasmas can be maintained for $\leqslant$300 ms and central electron densities, $n_e(0)$, and temperatures, $T_e(0)$, up to $1.7 \times 10^{19}\ \text{m}^{-3}$ and 2 keV, respectively, can be achieved, albeit not simultaneously while the central ion temperature, $T_i(0)$, is $\leqslant$80 eV. Steerable in-vacuum mirrors allow power from each gyrotron to be delivered independently to pre-programmed radii [26]. Additional heating is provided using two tangential NBI systems operated in a counter/co-counter configuration [27]. With these, 1 MW can be injected for up to 120 ms and $n_e(0)$, $T_e(0)$, and $T_i(0)$ up to $5 \times 10^{19}\ \text{m}^{-3}$, 400 eV, and 120 eV, respectively, are achieved.

2.1. Pellet injection set-up

A four-pellet pipe-gun type pellet injector system is operated on TJ-II [28]. It is fitted with a cryogenic refrigerator system for *in situ* pellet formation (hydrogen is used), fast propellant valves for pellet acceleration, in-line diagnostics to determine pellet velocity (light emitting/sensitive diode) and mass (in-line microwave resonance cavity), plus straight delivery lines (resulting in little or no mass loss due to friction) that deliver pellets to the plasma outer edge. See figure 1. Although 4 pellet sizes are available, only 0.66 mm and 0.76 mm diameter pellets are considered here. Four injection lines, termed *line*-1 through to *line*-4, are available. These are separated vertically and horizontally by 54 mm [29]. In this work, in which only *line*-1 and *line*-4 are employed, pellet flight paths pass close to the plasma axis, i.e. at $\rho = 0.05$, where $\rho = r/a$ is the normalized plasma radius. In addition, an injector for tracer encapsulated solid pellets (TESPEL) is sometimes piggybacked to the upstream end of *line*-4 (the pellet formation barrel is replaced by a tube with 1 mm inner diameter) [30]. With this set-up, these solid polystyrene pellets, drilled out and filled with a tracer impurity of interest, are injected at velocities between $\sim$200 and $\sim 400\ \text{m s}^{-1}$.

Direct optical access to the pellet/plasma interaction volume is possible via viewports located above (TOP) and behind (SIDE) the pellet flight path through the plasma [31]. See figure 1. Balmer Hα light signal (at 656.3 nm) emitted by the neutral cloud that surrounds an ablating pellet is collected using fibre-optic cables fitted with narrowband interference filters (centred at 660 +/− 2 nm with full-width at half-maximum of 10 nm) that are positioned outside these ports. In this case, the light is transferred to switchable gain amplified silicon diodes with bandwidth set to between 45 and 150 kHz. Next, the collection solid angle, viewport, fibre and filter transmission losses, detector efficiency, and amplifier gain are used when estimating a radial Balmer Hα emission profile (photons per second emitted by the neutral cloud). Finally, pellet penetration depth into plasma as a function of time can be determined from pellet velocity and knowing the microwave resonance cavity to plasma edge distance. For this it is assumed that pellets are neither accelerated nor decelerated while travelling along a guide-tube or through the plasma. The latter was confirmed using a fast-frame imaging camera [31, 32].

2.2. Plasma diagnostics

TJ-II is equipped with a large number of passive and active plasma diagnostics [33]. The diagnostics of interest here are a Thomson scattering (TS) system that provides one set per discharge of high spatial resolution electron density and temperature profiles [34], a microwave interferometer, a 16-channel electron cyclotron emission (ECE) system [35], Mirnov coils [36], plus two recently installed helicoidal arrays of magnetic pick-up coils. See figure 2. The microwave-based systems, with 10 μs temporal resolution, provide time traces of line-averaged electron density and electron temperature, respectively, along a discharge. In particular, the ECE system measures 2nd harmonic emission in X-mode polarization, from 49 to 64 GHz, and provides measurements at radial positions between $\rho = 0.7$ and 0. In the case of the single pulse ($\leqslant$40 ns, 8 J) TS system, its laser chord traverses the complete plasma. However, due to viewing geometry and signal intensity considerations, profiles are restricted to $\rho \leqslant \sim 0.8$. ECE signals are calibrated with the TS temperature profile to obtain temperature profiles along discharges.

Now, with regard to magnetic diagnostics, a Mirnov coil consisting of a straight array is positioned above the plasma column in sector C5, which is located at 113.5° toroidally from the PI. Next, two new arrays of magnetic pick-up coils follow the helical field coil as it winds around the central field coil of this 4 period device [37]. Each array consists of 32 sets of equally spaced (angle-wise) coils with each set containing one poloidal, one radial and one toroidal coil with winding areas of $0.0141\ \text{m}^2$, that extend toroidally along one period, or quadrant, of the TJ-II device. Signals are collected with 10^{-6} s temporal resolution and digitized at 2048 bits with +/−1 V range. These arrays are positioned close to the plasma column, at $\sim$0.3 m from the magnetic axis for the standard configuration, and one is called *superior*, the other *inferior*. See figure 2. In order to protect the coils, each array is installed inside

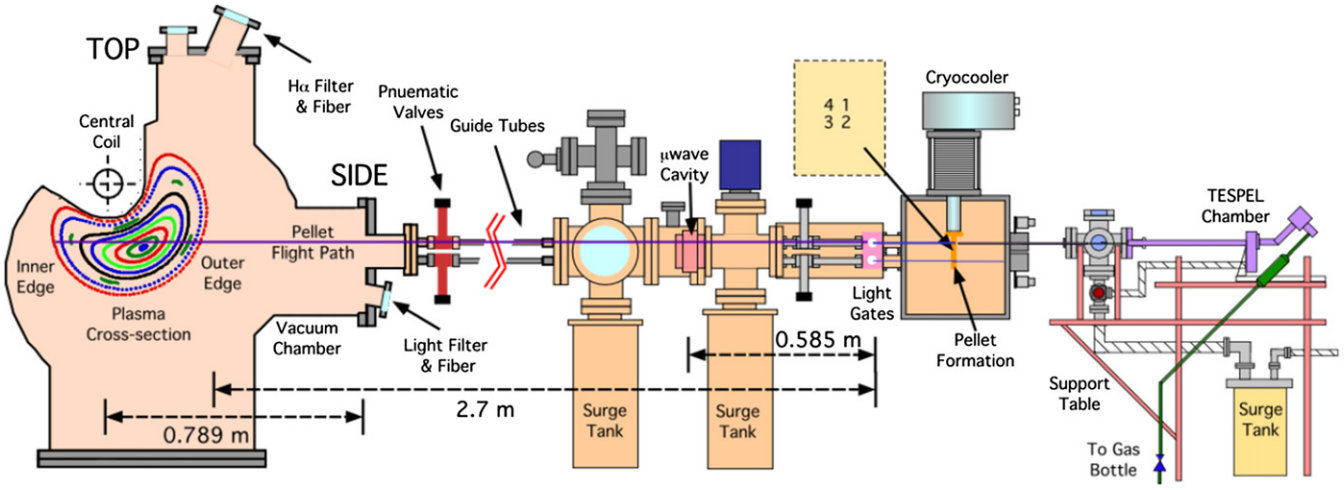

Figure 1. Sketch of TJ-II sector B2 plus the cryogenic pellet injector with a TESPEL injector connected to *line*-4. The locations of pellet guide tubes, in-line pellet diagnostics, and ablation light collection systems are indicated. The relative locations of *lines*-1 through to −4, when viewed from the rear end of the injector, are highlighted. The flight path through the plasma (magenta) for a pellet injected along *line*-4 is shown, as are closed magnetic flux surfaces for the configuration 100_44_64.

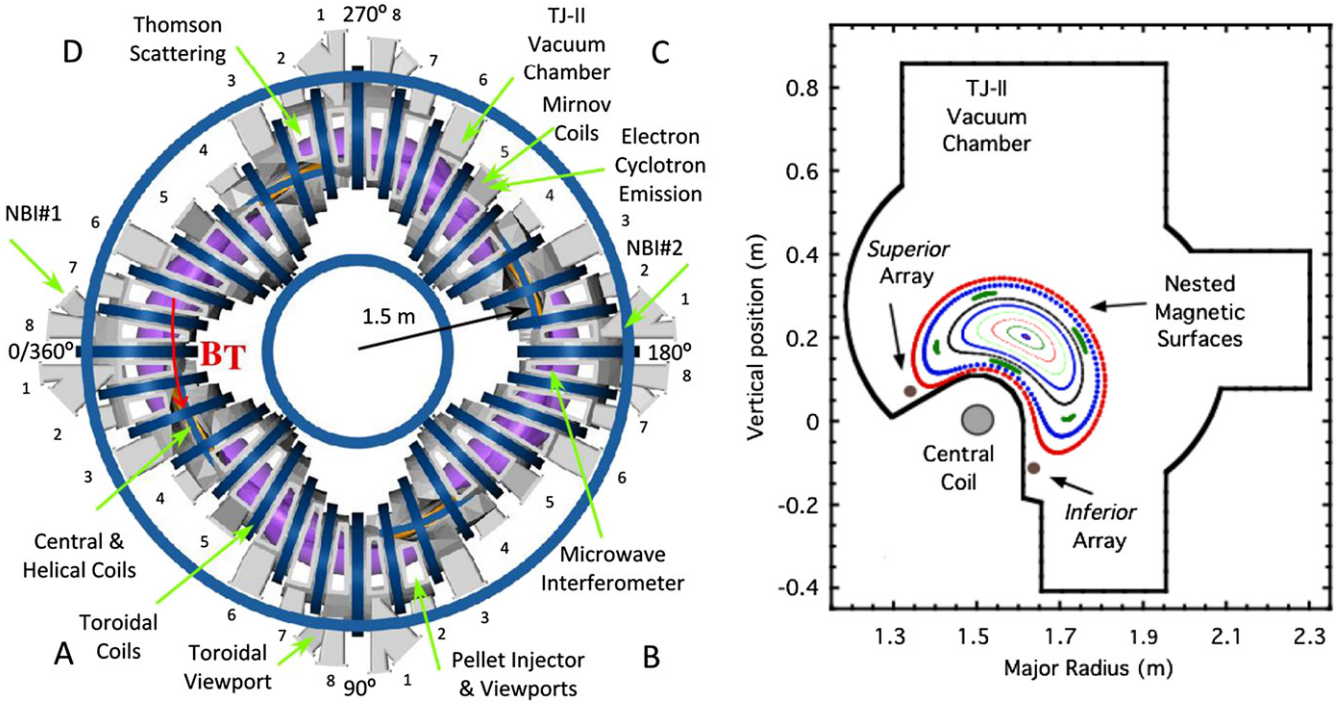

Figure 2. (*lhs*) Bird's-eye view sketch of the stellarator TJ-II. Locations of cited diagnostics as well as of quadrants A through to D and sectors 1 to 8 of each quadrant are indicated. The toroidal magnetic field direction is anti-clockwise. (*rhs*) Cross-sectional cut through sector D7. The locations of the toroidal magnetic arrays *inferior and superior* are shown.

corrugated stainless steel tubing (type 316 L) that is fixed to the chamber hardcore. For these experiments, signals from nearly all poloidal and radial coils plus a limited number of toroidal coils are collected and digitized at 1 MHz.

2.3. Pellet ablation and plasmoid drift

As a pellet enters plasma it's surface is initially directly ablated as background plasma particles (electrons and ions) impact on it. It is subsequently shielded from further direct interactions by a neutral cloud that develops about it. The ionized part of this cloud (plasmoid) expands along the magnetic field lines, while simultaneously detaching and drifting down the magnetic field gradient [38]. In the initial stage of pellet cloud expansion, energy transport is much faster that particle transport with the result that the plasmoid temperature equalizes rapidly with the background plasma temperature as plasma heat flux impinges on it. In contrast, the plasmoid particle density evolves more slowly, so an over-pressure develops. This pressure gradient drives plasmoid expansion

along the magnetic field line direction. Thereafter, changes in the particle velocity distribution produced by this expansion increases plasmoid acceleration whereas Alfvén wave emissions from both ends of this expanding plasmoid, which results in plasmoid charge loss via parallel currents, reduce drift acceleration.

In a stellarator, the magnetic field gradient does not align with the device major radius, rather its direction and magnitude vary along the magnetic field lines. So, a ∇B-drift of charged particles within the plasmoid induces an uncompensated ∇B current within the plasmoid, $j_{\nabla B}$, this being proportional to the pressure difference between the plasmoid and background plasma [39]. This $j_{\nabla B}$ current is cancelled by the development of an effective polarization current, $j_{\rm pol}$, given by $(n_0\, m_{\rm i})/{B_\infty}^2)$ $\delta E_0/\delta t$, where n is density, $m_{\rm i}$ is ion mass, E is the electric field that results from charge separation inside the plasmoid, and the subscripts 0 and ∞ refer to cloud and background plasma, respectively [39]. Now, solving for the short circuit condition, $j\nabla B + j_{\rm pol} = 0$, the time evolution of the resulting radial drift for a non-axisymmetric device is obtained as

$$\delta V_{\rm d}/\delta t = -2\,(p_0 - p_\infty)\nabla_\infty B_\infty / n_0 m_{\rm i} B_\infty, \qquad (1)$$

where p is pressure (in units of Pa), and $\nabla_\perp B_\infty/B_\infty$ is the inverse cross-field gradient scale-length [38]. This indicates that drift acceleration should continue until p_0 and p_∞ balance. In contrast, for tokamaks, assuming that the toroidal field is much stronger that the poloidal field then the term $\nabla_R B_\infty/B_\infty$ in equation (1) can be approximated by $1/R$, where $\nabla_R = \delta/\delta R$. In the TJ-II, the cross-field gradient scale-length, $L_B = B_\infty/\nabla_\perp B_\infty$, is close to 1 m^{-1} across the plasma region where pellets and TESPELs are injected [23], whereas in the same region, R varies from ~1.3 m at the inner plasma edge to ~1.75 m at the outer edge. Hence it is considered that the ∇B drifting in TJ-II will be larger that in an equivalent aspect ratio tokamak.

Finally, some additional effects related to short-circuiting of external and internal currents also reduce plasmoid acceleration, these being internal circuit closure (ICC) and external circuit closure (ECC), respectively [40, 41]. Their effect is to modify plasmoid drift and hence contribute to changing the deposited particle profile with respect to the ablation profile. Indeed, ECC is predicted to dominate drift-damping processes in tokamaks whereas ICC should dominate in stellarators [42]. Nonetheless, it is predicted that the strength of the ECC damping effect is enhanced in the vicinity of rational magnetic flux surfaces, in particular for tokamaks [43]. However, only a small enhanced damping effect is expected for stellarators due to the relative reduction in the importance of ECC damping with respect to ICC damping in such devices.

3. Transient magnetic activity

In order to summarize the magnetic activity observed during and immediately after the ablation phase of pellet injections, representative injections and signals are presented in subsections 3.1 to 3.3 for the standard TJ-II magnetic configuration, 100_44_64. In this configuration, $V_{\rm plasma} = 1.1$ m^3, $a = 0.192$ m, $B_0 = 1$ T and $1.551 \leqslant \iota/2\pi \leqslant 1.65$ in vacuum. Examples are presented for both ECRH and NBI-only heated plasmas and for solid hydrogen pellet and TESPEL injections.

3.1. H_2 pellet into ECRH plasma

In a first example, a cryogenic pellet with 7.3×10^{18} H atoms is injected at 924.2 m s^{-1} into ECRH target plasma having a line-averaged electron density of 4.4×10^{18} m^{-3}. See figure 3(*a*). Then, towards the end of the ablation phase (when the pellet has penetrated inside $\rho = 0.5$), periodic variations in light emission are apparent in the Balmer Hα emission profile recorded by a silicon diode with 150 kHz bandwidth that is located in the same machine sector. These features, called striations, are due to periodic detachments of the partially ionized neutral cloud from the pellet [7]. See figure 3(*b*). Next, returning to figure 3(*a*), plasma electron temperature and density begin to decrease and increase, respectively, as ablation nears completion. Looking again at this same figure, fluctuations in the magnetic signal plotted here (poloidal coil H4P32 located in sector D8 of TJ-II at toroidal angle $\phi = 360^\circ$ of figure 2) strengthen significantly towards the end of the ablation phase and remain stronger than pre-injection levels for more than 100 μs. When this signal is analyzed using a FFT procedure these fluctuations appear as increased activity in the frequency range below ~100 kHz. See figure 3(*c*). Finally, a significant reduction in broadband magnetic fluctuations occurs immediately after pellet ablation has terminated. In this case, the signal RMS decreases from 0.0134 V to 0.003 V in the range 50 to 500 kHz. See figure 3(*c*). This reduction lasts for several milliseconds before recovering again to pre-injection levels. The possible relationship between the Hα oscillations and magnetic oscillations in figure 3(*b*) and the post-injection reduction in broadband magnetic fluctuations in figure 3(*c*) are discussed in section 4.

3.2. H_2 pellet into NBI-heated plasma

In a second example, a cryogenic pellet is injected into NBI-heated plasma having line-averaged density and central electron temperature of 1.9×10^{19} m^{-3} and ~300 eV, respectively. The pellet contains 2.2×10^{19} H atoms, its velocity is 709.1 m s^{-1} and it penetrates beyond the magnetic axis to reach the inner plasma edge. See figures 4(*a*) and (*b*). Due to cooling of the plasma by the pellet, the pellet ablation rate reduces after it crosses the magnetic axis and striations, which are visible before this, fade into the Balmer Hα light signal. In this case, a strong oscillation is observed in the H4P32 magnetic pick-up coil signal before the pellet crosses the magnetic axis. However, this oscillation decays once the pellet crosses to the inner plasma region. Now, when the H4P32 signal is analyzed using the FFT procedure increased magnetic activity is seen in the frequency range below ~100 kHz, as found in the ECRH case. Finally, a reduction in broadband magnetic fluctuations is also observed for several milliseconds after pellet injection into NBI-heated plasma. See figure 4(*c*). However, this reduction is significantly lower that measured for ECRH plasma. In the NBI case, the signal RMS decreases from 0.01 V to 0.007 V immediately after the pellet injection in the range 50 to

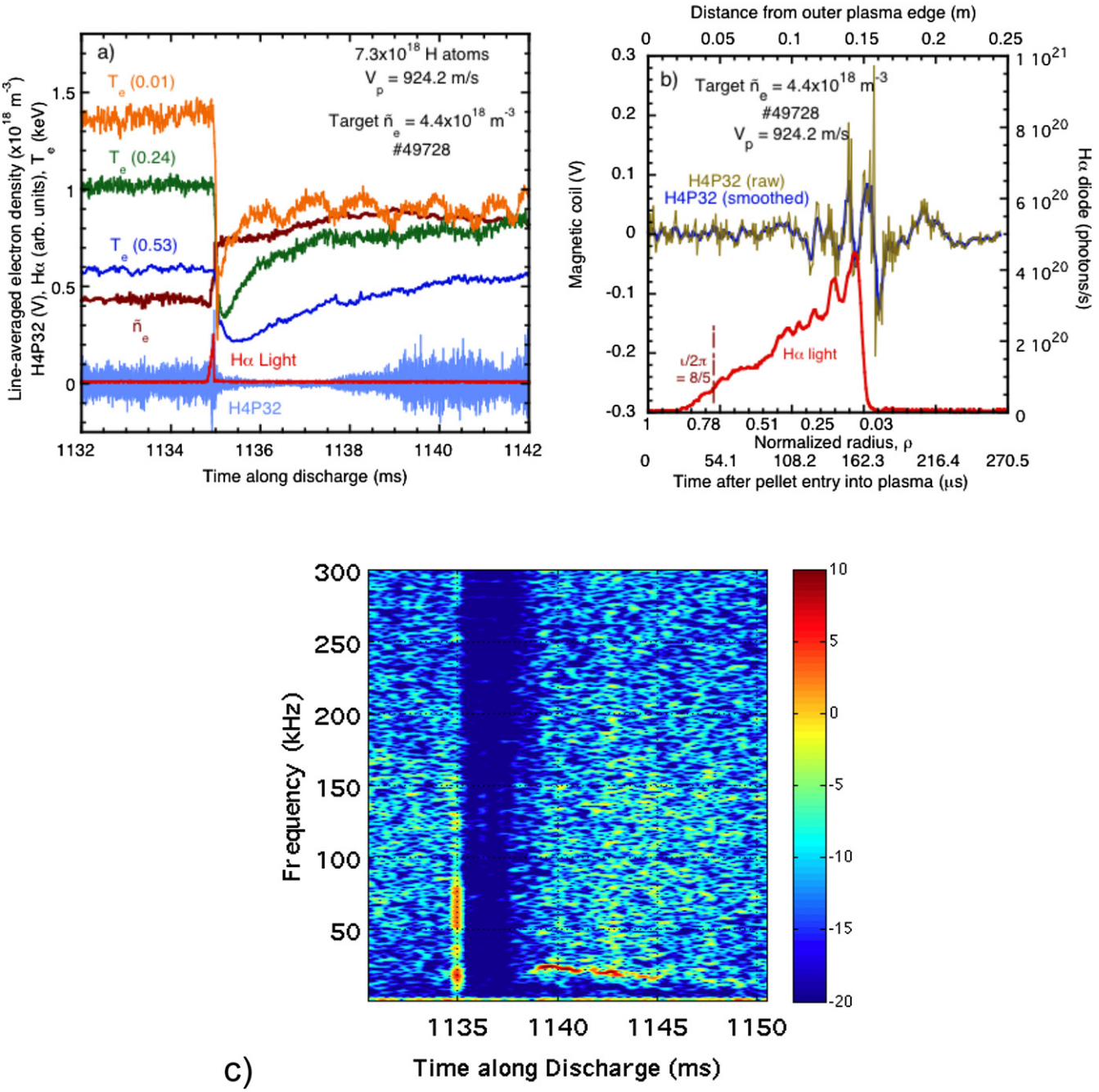

Figure 3. Injection of a hydrogen pellet with 7.3×10^{18} H atoms into ECRH discharge #49728 having target line-averaged electron density $= 4.4 \times 10^{18}$ m^{-3}. (*a*) Time evolution of $\tilde{n}_e$ (brown), H4P32 magnetic coil signal (light blue), and ablation Hα light emission (red) plus T_e at several radii. (*b*) Traces of Hα light emission (red) plus raw and smoothed output from the poloidal H4P32 magnetic coil (blue and olive) as a function of time after pellet entry into plasma, normalized radius, and distance into plasma. (*c*) H4P32 magnetic spectrograph as a function of time along the discharge. The colour bar represents $\log_{10}$(power). The pellet enters the plasma at 1134.798 ms.

500 kHz before increasing again to the pre-injection level 6 to 7 ms later.

3.3. TESPEL into ECRH plasma

As a third example, a tracer-loaded polystyrene $(\text{-}C_8H_8\text{-})_n$ sphere (TESPEL) [3] is injected into ECRH heated plasma having a line-averaged density of 4×10^{18} m^{-3}. See figure 5(*a*). The TESPEL is 300 μm in diameter, it is loaded with several micrograms of aluminium tracer, and it achieves a velocity of 365.2 m s^{-1}. See figure 5(*b*). As for cryogenic pellets, the TESPEL ablation rate is determined mainly by local electron temperatures and densities along its flight path [23]. However, Balmer Hα light emission is reduced significantly due to the lower density of H atoms in its neutral clouds. The aluminium tracer, located in the core, is exposed to the plasma once the polystyrene has been ablated. This occurs between $\rho = 0.2$ and $\rho = 0.3$ (the narrow but intense light peak at the

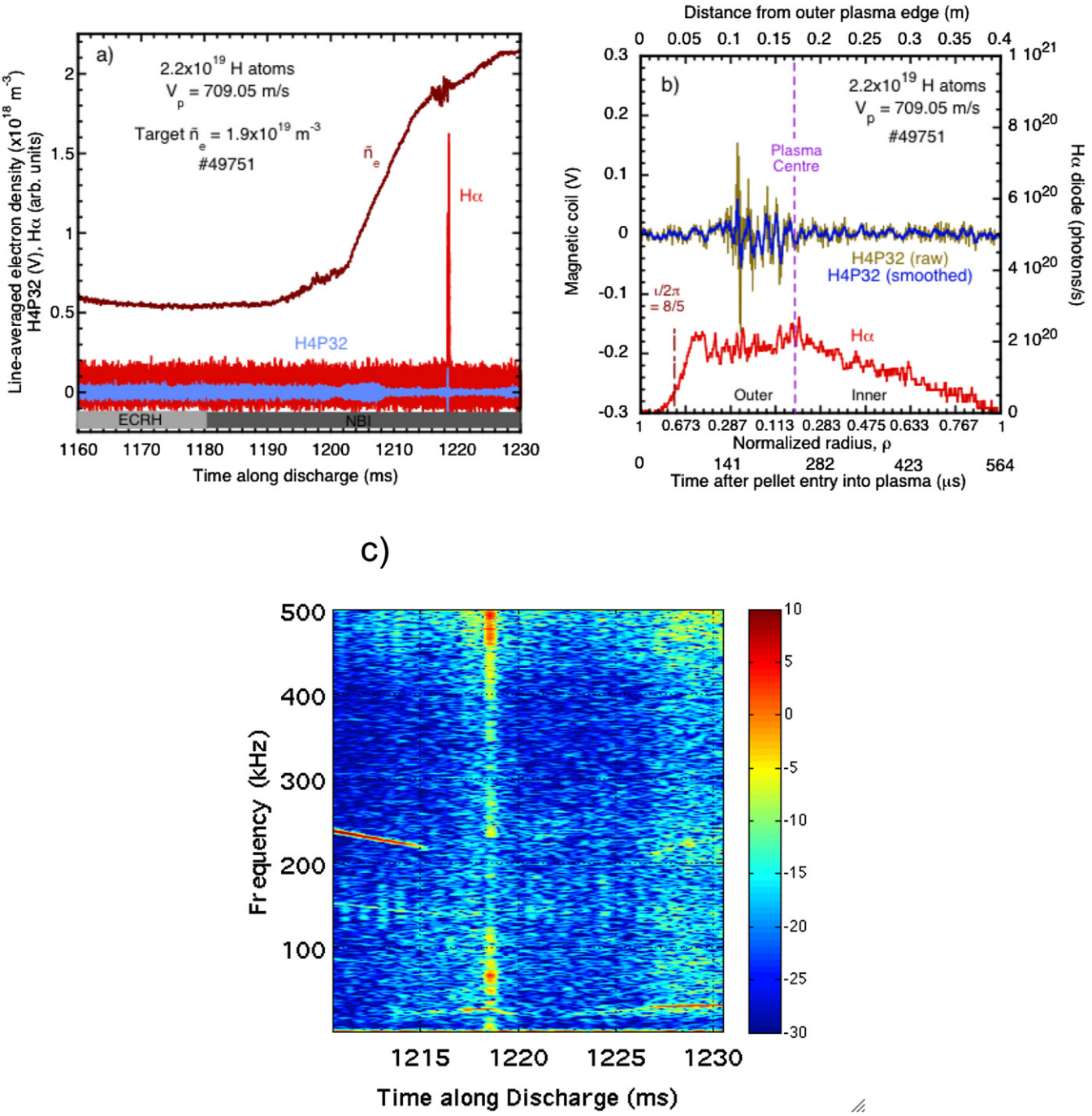

Figure 4. Injection of a hydrogen pellet with 2.2×10^{19} H atoms into the NBI-heated plasma discharge #49751 having target line-averaged electron density $= 1.9 \times 10^{19}$ m^{-3}. (*a*) Time evolution of $\tilde{n}_e$ (brown), H4P32 magnetic coil signal (light blue), and ablation Hα light emission (red). ECE signals are in cut-off for densities $\geqslant 10^{19}$ m^{-3}. (*b*) Traces of Hα light emission (red) plus raw and smoothed output from the poloidal H4P32 magnetic coil (blue and olive) as a function of time after pellet entry into plasma, normalized radius, and distance into plasma. (*c*) H4P32 magnetic spectrograph as a function of time along the discharge. The colour bar represents $\log_{10}$(power). The pellet enters the plasma at 1218.403 ms.

end of the ablation phase confirms that tracer deposition is well-localized radially). Although not apparent in this figure (the higher detector gain used limits its bandwidth to 45 kHz), plasmoid detachments occur for TESPELs at time intervals similar to those for cryogenic pellets (every 10 to 20 μs) [30]. However, neither an oscillation similar to that seen in figures 3 and 4 nor increased fluctuations at higher frequencies are seen in any magnetic signal recorded by Mirnov or helical array pick-up coils even though the pellet penetrates to the same plasma minor radius as the hydrogen pellet in figure 3(*a*). Nonetheless, as for the hydrogen pellet injected into the ECRH plasma, broadband magnetic fluctuations also diminish significantly for several milliseconds after this TESPEL injection. See figure 5(*c*). In this case, the signal RMS decreases from 0.032 V to 0.004 V in the range 50 to 500 kHz.

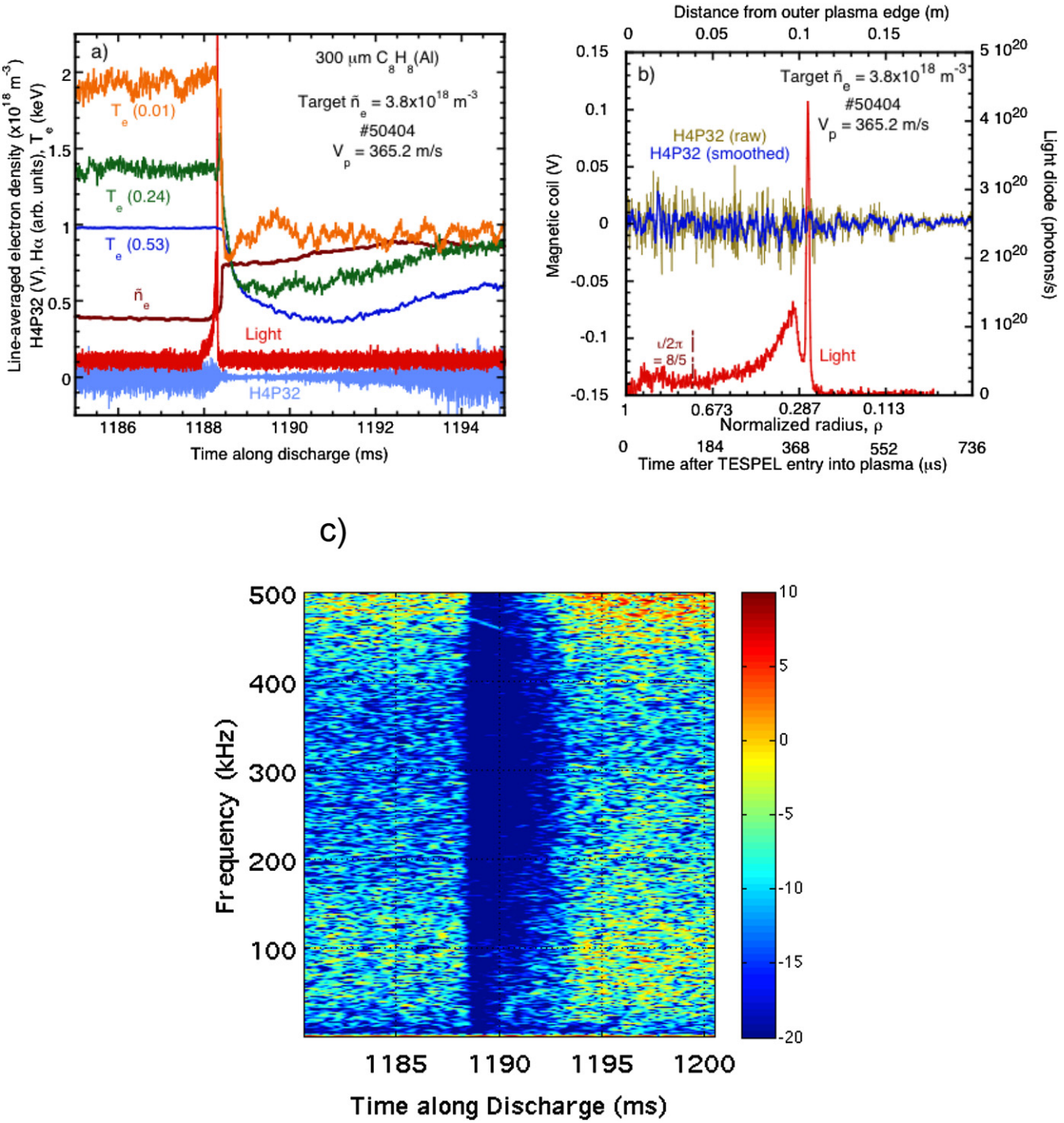

Figure 5. Injection of an aluminium-loaded TESPEL with 300 μm outer diameter into the ECRH plasma discharge #50404 having target line-averaged electron density $= 3.8 \times 10^{18}$ m^{-3}. (*a*) Time evolution of $\tilde{n}_e$ (brown), H4P32 magnetic coil signal (light blue), ablation light emission (red) plus T_e at several radii. (*b*) Traces of light emission (red) plus raw and smoothed output from the poloidal H4P32 magnetic coil (blue and olive) as a function of time after pellet entry into plasma, normalized radius, and distance into plasma. (*c*) H4P32 magnetic spectrograph as a function of time along the discharge. The colour bar represents $\log_{10}$(power). The TESPEL enters the plasma at 1187.912 ms.

3.4. Injection summary

It can be concluded from the observations presented here that a strong oscillation is excited in TJ-II magnetic signals by cryogenic pellets only, that the development of such an oscillation is independent of the heating method, that such oscillations are not observed when a pellet is traversing the plasma inner region, and that broadband magnetic fluctuations reduce significantly for several milliseconds after the injection of either pellet type with the largest reduction occurring for ECRH plasma. These phenomena are discussed in section 4.

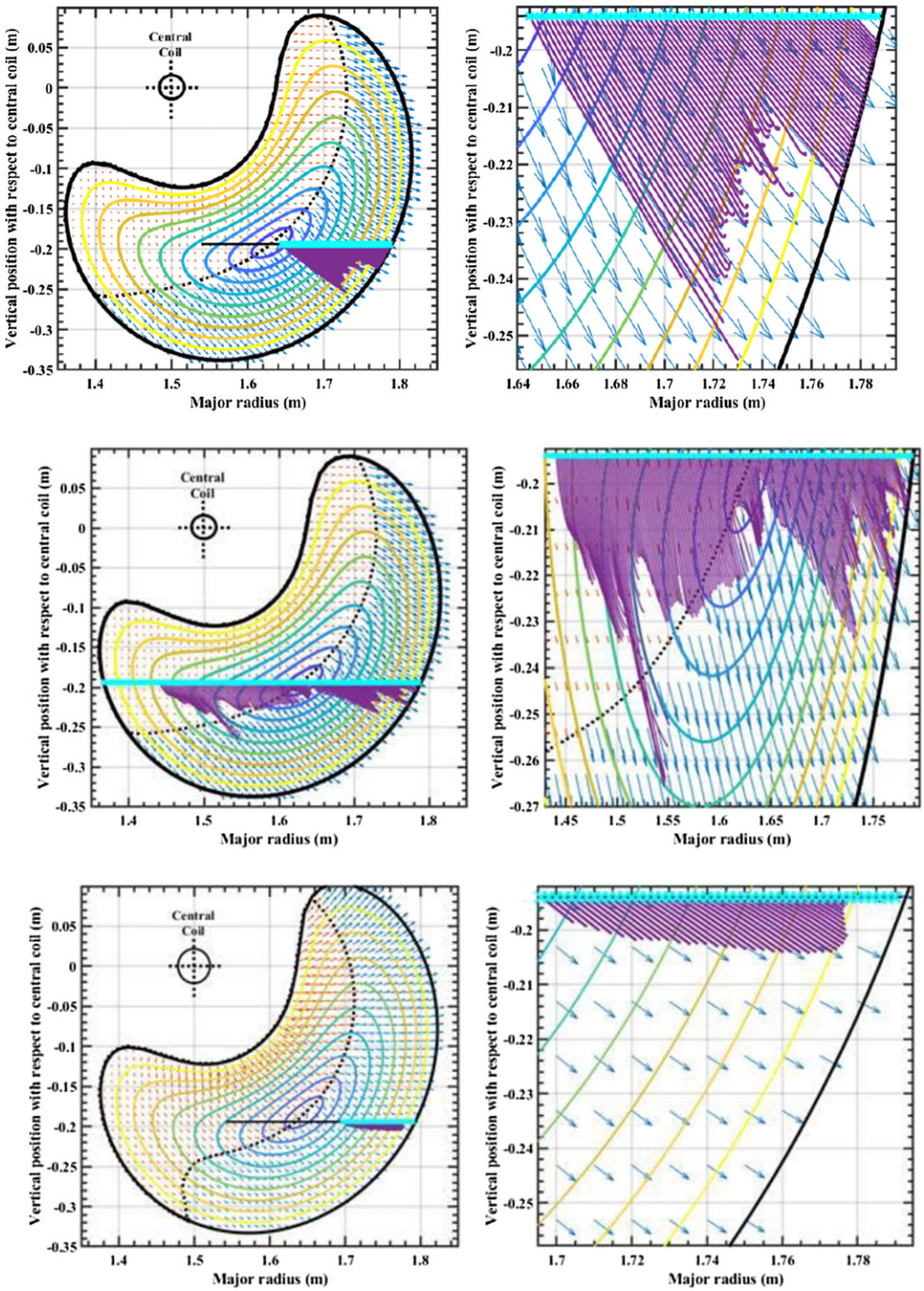

Figure 6. HPI2 simulations showing plasmoid acceleration (arrow lengths are proportional to acceleration) and trajectories (magenta) for pellet injection under different plasma heating conditions. Pellets are injected from right to left along a horizontal flight path (cian). Plots show the poloidal cross-section of sector B2 with closed magnetic flux surfaces for the 100_44_64 configuration (for $\rho = 0$ to 1 with $\Delta\rho = 0.1$ interspacing). (*Top lhs*) Simulation for a pellet with 7.3×10^{18} H atoms injected into ECRH discharge #49728. (*Top rhs*) Amplification of the outer plasma region. *Middle*: As *top* but for a pellet with 2.2×10^{19} atoms injected into NBI-heated discharge #49751. (*Bottom*) As *top* but for a TESPEL injected into ECRH discharge #50404. In all cases, individual calculations begin at equally spaced steps (2 mm) along the flight path. The pellet and its cloud are followed inwards from each step position until the cloud detaches. The detached plasmoid trajectory (magenta) is determined before the process returns to the next step position. This is repeated until the pellet is fully ablated.

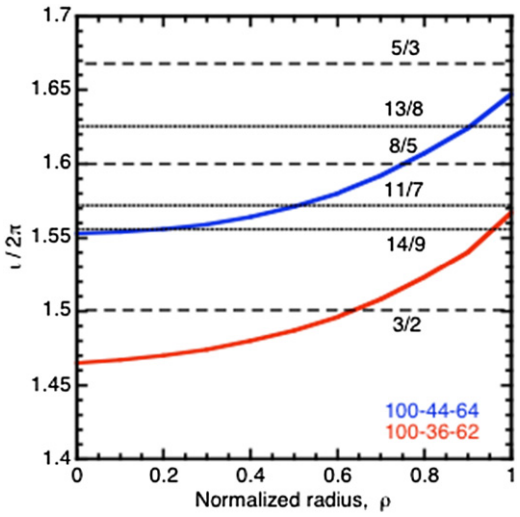

Figure 7. Normalized plasma radius versus rotational transform, $\iota/2p = n/m$, for TJ-II magnetic configurations of interest here. Principal rational surfaces are indicated.

4. Discussion

The transient magnetic activities described in subsections 3.1 to 3.3 are examined in more detail in subsections 4.1 to 4.3 and possible explanations for each effect are discussed. In addition, for completeness, an example discharge showing the impact of a cryogenic pellet on well-developed NBI-driven AEs is presented in subsection 4.4.

4.1. Strong oscillation

4.1.1. H_2 pellet into ECRH plasma. In section 3, the interaction of drifting plasmoids with a rational surface was forwarded as a probable explanation for the strong magnetic oscillation with frequency below ∼100 kHz during cryogenic pellet injections into TJ-II plasmas. This hypothesis can be alluded to here by comparing the strong oscillation in figure 3(*b*) with the Balmer Hα signal of the same figure as there appears, as first glance, to be some degree of coherence between the oscillation in the magnetic signal and striations in the Hα signals. For instance, the oscillation, which starts with a drop in magnetic signal, begins shortly after the first striation (falloff in light intensity) is discernible in the Balmer Hα signal and, thereafter, the time intervals between striations and valleys is similar, i.e. from ∼10 and ∼17 μs for the magnetic signal compared to between ∼9 μs and ∼16 μs for Balmer Hα. As mentioned in subsection 3.1, striations are due to detachments of partially ionized neutral clouds from a pellet. Once detached, plasmoids expand along the magnetic field lines, while simultaneously drifting down the magnetic field gradient, until plasmoid and plasma pressures equalize. In order to determine if drifting plasmoids can reach rational magnetic surfaces within the time ranges noted above a stellarator version of the pellet injection code HPI2 code is employed to simulate pellet injections in TJ-II [32, 43].

The HPI2 code simulates pellet ablation and homogenization of the ablated material in a consistent way. It considers target plasma density and temperature profiles as well as the specific geometrical data of the device and the magnetic configuration. Simulations made for the 100_44_64 configuration, where the effective inverse curvature radii are negative for the region between the plasma outer edge and the magnetic axis, show that resultant trajectories of all plasmoids detaching in this region will be outwards and downwards [32]. Indeed, the directions and magnitudes were confirmed experimentally for TJ-II by analyzing images of Balmer Hα emissions obtained using a fast-frame imaging camera [32]. In figure 6, it is found that, for the pellet parameters and the ECRH plasma conditions of figure 3, plasmoids that detach from the pellet when this is in the outermost plasma region ($\sim 0.9 \leqslant \rho \leqslant \sim 0.5$) reach the plasma edge with little or no interaction with rational surfaces whereas plasmoids that detach when the pellet is inside $\rho \leqslant \sim 0.5$ undergo abrupt drift deceleration in the proximity of the 8/5 rational surface located near $\rho = 0.75$ (abrupt deceleration is characterized here by a truncated upward drift in the magenta curves). See figure 7. In order to interpret this, it should be noted that, in stellarators, the ICC effect, referred to in subsection 2.3, is most effective close to the plasma edge and dominates plasmoid drifts for the region $\sim 0.9 \leqslant \rho \leqslant \sim 0.5$. In contrast, ICC may be reduced for plasmoids originating from $\rho \leqslant \sim 0.5$ thus allowing the second-order enhanced ECC damping effect, in which external electric potential reconnection lengths are significantly reduced in the vicinity of such a flux surface, to cause abrupt braking of plasmoid drifts [43]. Returning to the simulation in figure 6, it is found that the time needed for the complete homogenization of a plasmoid that detaches from the pellet at $\rho = 0.2$ is ∼51 μs. During the first ∼18 μs of this period the plasmoid drifts out to $\rho = \sim 0.71$, where it undergoes abrupt drift deceleration, while during the remaining 33 μs homogenization continues with little or no additional radial drift. This simulated drift time is in good agreement with the time interval between the final falloff in Hα light intensity and the last valley in the magnetic signal, i.e. ∼17 + /−4 μs (this is considered the experimental drift time).

4.1.2. H_2 pellet into NBI-heated plasma. In the NBI-heated plasma example in figure 4, the injected pellet penetrates through almost the whole plasma column to reach the region close to inner plasma edge. In this case, a strong magnetic oscillation is detected shortly before the pellet reaches the plasma centre and decays once the pellet has crossed the magnetic axis. In order to make an evaluation similar to that made for the previous case, the HPI2 code is used to simulate the pellet parameters and the NBI-heated plasma conditions of this figure. In this case it is necessary to recall that effective inverse curvature radii are positive in the region beyond the magnetic axis, thus plasmoid detaching there will drift downwards and towards the magnetic axis [32]. Returning to the simulation for NBI, in figure 6 the majority of plasmoids which detach from the pellet when this is in the outermost plasma region ($\sim 0.9 \leqslant \rho \leqslant \sim 0.5$) reach the plasma edge whereas plasmoids which detach in the region $\sim 0.5 \leqslant \rho \leqslant \sim 0.2$ undergo abrupt drift deceleration in the proximity of the 8/5 rational surface. In contrast, predictions show no apparent enhanced plasmoid deceleration in the vicinity of the 11/7 rational surface at $\rho = 0.5$,

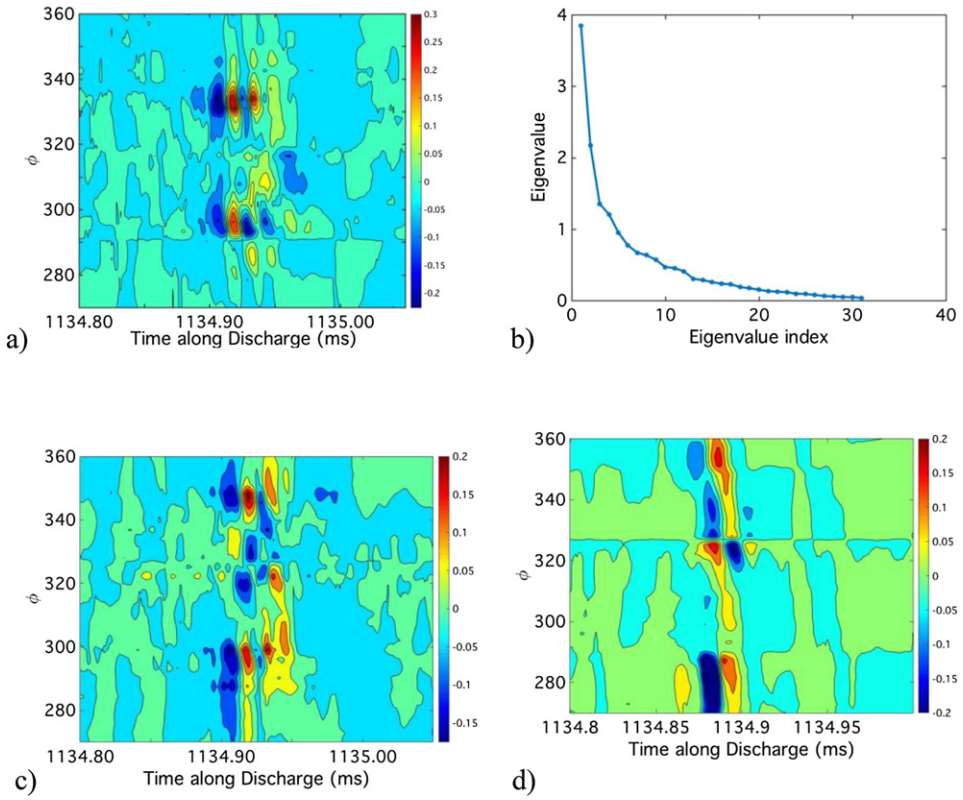

Figure 8. SVD reconstructions using 10 eigenvalues of signals from the polodial and radial coils of the toroidal array. Here ϕ is TJ-II toroidal angle, with 360° being closest to the pellet injector. (*a*) SVD reconstruction of signals from the *inferior* radial coils for a pellet with 6.4×10^{18} H atoms injected at 925.6 m s^{-1} into ECRH discharge #50407 having target line-averaged electron density of 3.8×10^{18} m^{-3} that was confined using the 100_44_64 configuration. The pellet enters the plasma at 1134.793 ms and is fully ablated at 1134.933 ms. (*b*) Eigenvalue versus eigenvalue index for the SVD of (*a*). (*c*) SVD reconstruction of signals from the *superior* poloidal array for discharge #50407. (*d*) SVD reconstruction of the *superior* poloidal array for a cryogenic pellet with 5.6×10^{18} H atoms injected at 929.9 m s^{-1} into the ECRH discharge #50426 having target line-averaged electron density of 3.4×10^{18} m^{-3} that was confined using the 100_36_62 configuration. The pellet enters the plasma at 1134.745 ms and is fully ablated by 1134.89 ms.

albeit enhanced deceleration may be occurring close to the 14/9 rational surface at $\rho = 0.2$ for plasmoids that detach in the inner plasma region between $\rho = 0$ and $\rho = 0.15$. Finally, plasmoids that detach on the inner side of this $\rho = 0.15$ are seen to be unaffected by rational surfaces. The simulations are in good agreement with the experimental results presented in subsection 3.2 in which it was observed that the strong oscillation in the H4P32 magnetic signal decayed once the pellet had crossed the magnetic axis.

4.1.3. TESPEL into ECRH plasma. Finally, in order to understand the absence of enhanced magnetic oscillations during TESPEL ablation it should be recalled that drift accelerations of detached C_8H_8 plasmoids are reduced by a factor $1/m_i$, i.e. where $m_i = (12 + 1)/2 = 6.5$ [23]. Moreover, plasmoid pressures are significantly lower than those of cryogenic pellets since C_8H_8 plasmoid electron densities are low (inner electrons are tightly bound to carbon so ionization to C^{+6} requires several milliseconds [23]), hence C_8H_8 plasmoids reach equilibrium with the background plasma more quickly than those originating from a H_2 pellet. Hence, outward drift lengths should be much shorter than for cryogenic pellets, hence C_8H_8 plasmoids should cease drifting before reaching a rational surface of interest. This argument for short TESPEL drift lengths is confirmed by comparing post-injection TS density profiles for both pellet types injected into similar ECRH plasmas, i.e. TESPEL profiles peak close to the plasma centre whereas H_2 profiles are shifted towards the plasma edge [23]. Indeed, HPI2 simulations further support these arguments. In figure 6, outward drift lengths for TESPEL plasmoids are severely abbreviated when compared to those for hydrogen and no appreciable deceleration is predicted in the proximity of rational surfaces.

4.1.4. Plasmoid interaction with rational surfaces. Plasmoid interaction with the 8/5 resonant surface at $\rho = 0.75$ is considered the prime candidate to explain the strong oscillations found here in magnetic signals. In order to reinforce this affirmation, it is necessary to confirm experimentally that this resonant surface is being excited. The magnetic signals presented in figure 3 through to 5 are from a single poloidal coil, H4P32, which belongs to the *superior* array of newly installed pick-up coils. Each of these arrays, with 32 coil sets, extends along the full length of quadrant *D* (from $\phi = 270°$ to 360°) and follows the winding of the helical field coil that wraps around the central field coil. See figure 2. Thus, this set-up permits, for instance, the toroidal number of excited modes to

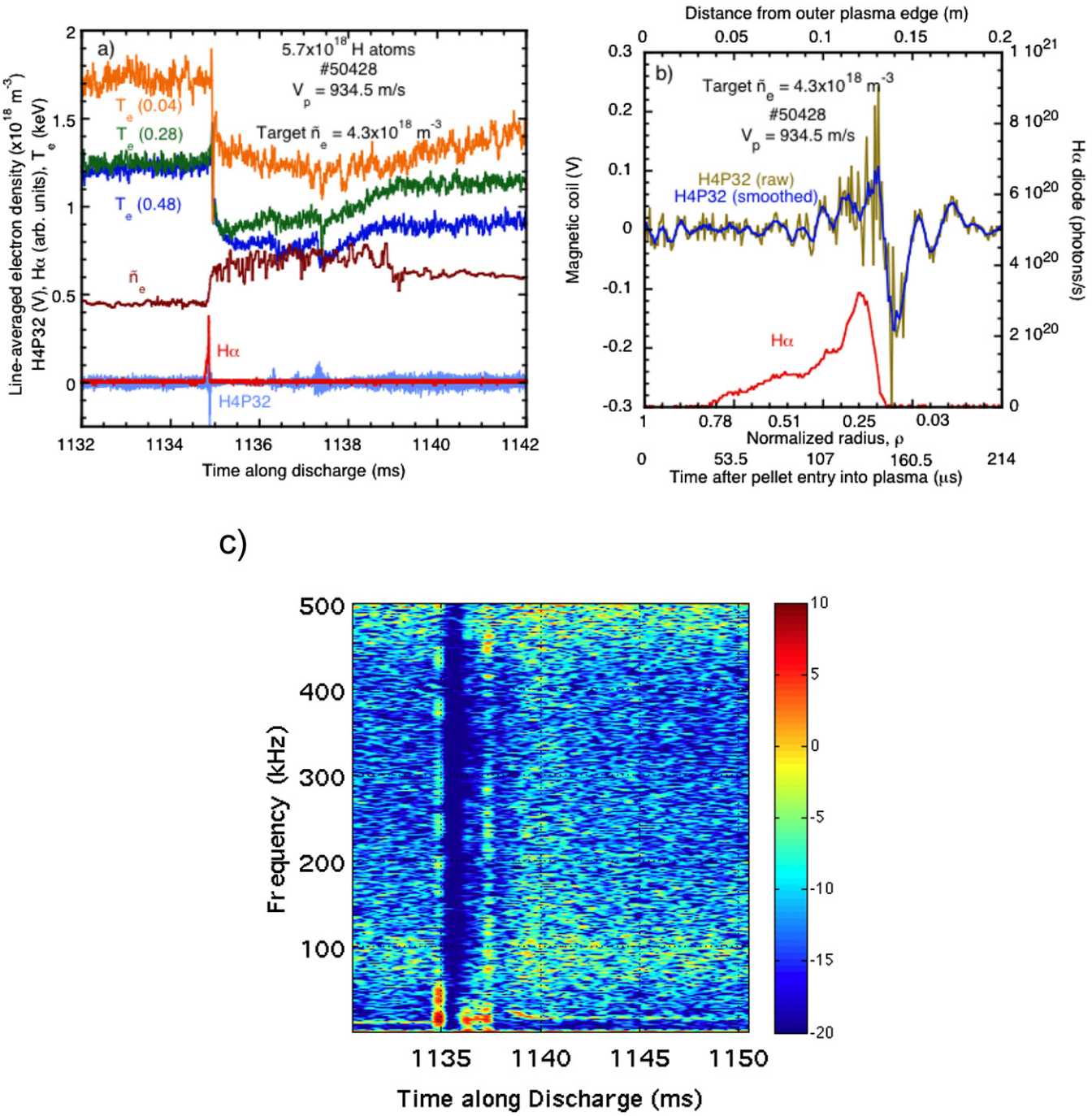

Figure 9. Injection of a hydrogen pellet with 5.7×10^{18} H atoms into ECRH plasma discharge #50428 made with magnetic configuration 100_36_62 having target line-averaged electron density $= 4.3 \times 10^{18}$ m^{-3}. (*a*) Time evolution of $\tilde{n}_e$ (brown), H4P32 magnetic coil signal (light blue), and ablation Hα light emission (red) plus T_e at several radii. (*b*) Traces of Hα light emission (red) plus raw and smoothed output from the poloidal H4P32 magnetic coil (blue and olive) as a function of time after pellet entry into plasma, normalized radius and distance into plasma. The light diode bandwidth is set to 45 kHz. (*c*) H4P32 magnetic spectrograph as a function of time along the discharge. The pellet enters the plasma at 1134.733 ms. Small pieces of ice also enter the plasma at 1136.344, 1136.8 y 1137.355 ms and perturb the H4P32 signal, as seen in (*a*) and (*c*).

be determined. In order to extract the dominant mode, the singular value decomposition (SVD) method is used, permitting a clear reconstruction of the spatiotemporal mode structure from multi-coil data. This technique is applied to signals from one of the magnetic pick-up coil types for a 250 μs long time window centred about the pellet injection time. The largest 10 eigenvalues are used to extract the dominant oscillations from the fluctuation data [44, 45]. See figure 8. Here 10 eigenvalues constitute ∼98% of the 'fluctuation energy', the rest is considered as noise [44]. In figures 8(*a*) and (*c*), SVD plots are reconstructed using signals from 31 of the 32 radial coils of the *inferior* array and from 31 poloidal coils of the *superior* array (the coils at 304.8° do not function), respectively, for a cryogenic pellet injected

into the 100_44_64 configuration. In these cases, the toroidal separation between maxima is $\phi = \sim 40^\circ$ and $\sim 50^\circ$ for the *inferior* and *superior* arrays, respectively. Here, an average value is taken in order to correct for any angular displacements as the arrays extend along the toroidal sector. It should be noted that the weak mode that appears at $\sim 322^\circ$ before injection in figure 8(*c*) is amplified during the ablation phase. However, it is not seen in figure 8(*a*) so its origin is unclear. Then taking the above limits for ϕ, the toroidal n mode excited by the pellet is between 7 and 9. Finally, from figure 7, it is considered that the 8/5 rational surface is the most likely candidate. However, other rational surfaces such as the 11/7 cannot be ruled out completely as some uncertainty exists. For comparison, the plot in figure 8(*d*) is for a hydrogen pellet injected into ECRH plasma created with the 100_36_62 magnetic configuration. See also figure 9. For this configuration, V_{plasma} is 1 m^3, a is 0.184 m, B_0 is 1 T, and $1.47 \leqslant \iota/2\pi \leqslant 1.57$, so a 3/2 rational surface is located at $\rho = 0.63$ while a 14/9 rational surface is located at $\rho = 0.95$. See figure 7. Returning to figure 8(*d*), the toroidal angular separation between excited modes is $\sim 32.5^\circ$. This corresponds most closely to the rational surface 11/7 that is just outside the last-closed flux surface of this configuration. Given that a large fraction of pellet particles are swept outwards and lost to the plasma this may be reasonable. Finally, in other SVD plots for 100_36_62, not shown here, only a single excited mode is observed at $\sim 320^\circ$. In such cases it may be the 3/2 rational surface only, at $\rho = 0.63$, that is excited.

Finally, in order to understand how oscillations are induced in magnetic signals by outward drifting plasmoids, it is considered that an abrupt steepening of the local radial pressure gradient can arise when a cold high-density plasmoid is deposited in close proximity to a rational surface. This in turn can give rise to a magnetic instability that leads to a variation in the local magnetic field. Such an instability will be short lived and magnetic reconstruction will occur once homogenization is completed and the pressure gradient reduces. A train of such plasmoids being deposited at the same location will give rise to a continuous variation of the local radial pressure gradient and an oscillating magnetic signal. This will be maintained as long as plasmoids continue to reach the same rational surface, otherwise it will become damped.

An alternative explanation for the oscillations in magnetic signals is that these are due to a rotating mode. Indeed, modes are expected to rotate with plasma fluid if plasma temperature is sufficiently high [46]. Thus, if an outward drifting plasmoid induces an island located close to a rational surface to grow, its rotation, which mirrors the plasma fluid rotation, should be observable in magnetic coil signals. Thereafter, as the island shrinks, its signal will decay. In figure 3(*c*), the frequency range of the oscillation in the H4P32 signal is between ~ 55 and ~ 80 kHz. If this corresponds to an island close to the 8/5 rational surface at $\rho = 0.75$, then following the arguments in reference [46] to estimate poloidal rotations of modes in TJ-II, $V_\theta \simeq 2\pi\,\rho\,\text{an}\,f/m$ where f is mode frequency and $m = 5$, gives $V_\theta = 9.7$ to 14.5 km s^{-1}. For this, approximate circular geometry is assumed, which results in an uncertainty of $\sim 20\%$. When compared with experimental measurements made in TJ-II for similar ECRH plasmas [47], these calculated V_θ values are 2.5 to 3.7 times higher than experimental values. This would imply that a rotating mode is probably not the source of the ~ 55 to ~ 80 kHz oscillation in H4P32 that occurs during pellet ablation. However, the short-lived mode that appears at lower frequencies during pellet ablation in figure 3(*c*), i.e. between $f = 13$ and 22 kHz, could be associated with a rotating island since the corresponding V_θ, 2.4 to 4 km s^{-1}, is in good agreement with experimental poloidal rotation measurements [47]. Finally, the mode that appears soon after pellet injection with $f = 20$ to 25 kHz in the same figure, i.e. between 1139 and 1145 ms, may also corresponds to a rotating mode since $V_\theta = 3.7$ to 4.6 km s^{-1} also agree well with measurements in TJ-II [47]. A mode, with a similar frequency, also appears after pellet injection in figure 9(*c*).

4.2. Transitory post-injection reduction in fluctuations

It is seen in figures 3(*c*), 4(*c*), 5(*c*) and 9(*c*) that a reduction of broadband magnetic fluctuations occurs immediately after a pellet injection and that this reduction is strongest for ECRH plasmas. This weakening in magnetic fluctuations lasts for several milliseconds before recovering again to pre-injection levels. In the case of ECRH plasmas, the reduction in broadband magnetic fluctuations appears to be related to the rapid drop in T_e rather than to the two-stage increase in line-averaged electron density, $\sim\tilde{n}_e$, i.e. an initial fast increment in $\tilde{n}_e$ followed by a slow upward growth to maximum. This is most apparent for the TESPEL injection into ECRH discharge #50404, figure 5(*a*), where the drop in T_e is large (from 2 to 0.8 keV at $\rho = 0$) and instantaneous (within ~ 300 μs) whilst after an initial fast jump, $\Delta\tilde{n}_e = 3.7 \times 10^{18}$ m^{-3}, $\tilde{n}_e$ grows to a maximum (with $\Delta\tilde{n}_e = 5.2 \times 10^{18}$ m^{-3}) after several milliseconds as higher ionization states of carbon and the tracer (Al) release their electrons to the plasma [21]. Similar time traces are seen for T_e and $\tilde{n}_e$ for the cryogenic pellet in figure 3. In ECRH plasmas, broadband magnetic fluctuations return to pre-injection levels 4 to 5 ms later, i.e. before T_e and $\tilde{n}_e$ have returned to pre-injection values. In contrast, it is not possible to repeat this evaluation for NBI-heated plasma as ECE signals are in cut-off prior to pellet injection. Moreover, broadband magnetic fluctuations are already significantly reduced prior to pellet injection in figure 4 and the relative reduction in broadband fluctuations is much less than for the ECRH case. However, a full understanding of post-injection broadband magnetic fluctuation recovery remains outstanding at present for both situations.

4.3. Alfvén emissions

As mentioned in subsection 2.3, Alfvén wave emission occurs from the tips of plasmoids as these expand along magnetic field lines [43]. Alfvén emission frequencies can be estimated as $f_{AE} = \omega_{AE}/2\pi$ where $\omega_{AE} = V_A/2qR$ with $V_A = B/\sqrt{(\mu_0 \Sigma_i n_i m_i)}$ for SI units, μ_0 is permeability of the vacuum, n_i is ion density, m_i is ion mass, and $q = 2\pi/\iota = m/n$ [48]. Here, $B = 1$ T, $R = R_0 = 1.5$ m, $q = 0.61$ to 0.645 for the standard TJ-II configuration, and it is assumed that plasmoid ion and electron densities are equal. Preliminary results, using a

3 filter based spectroscopy system [49], indicate that the initial plasma-cloud electron density and temperature are close to 10^{23} m^{-3} and 1 eV, respectively, for a cryogenic pellet in TJ-II. Subsequently, as plasmoids expand along magnetic field lines and drift outwards, their density will reduce until pressure equilibrium is achieved with background plasma. Thus, for plasmoid ion densities from 10^{23} m^{-3} to lower densities, Alfvén wave emission should occur above ∼6 kHz and extend to several hundreds of kHz. However, there are no apparent frequency bands in figures 3(*c*), 4(*c*), 5(*c*) or 9(*c*) that could be attributed to such Alfvén wave emissions. Alternatively, the model for Alfvén wave emissions from expanding pellet clouds by Parks *et al* [50], based on work by Drell *et al* [51], could be considered. In this case, the Alfvén frequency is determined for a moving source of dimension L along its velocity with speed V, from $\omega_{AE} \sim V/L$. In this case, using representative values for TJ-II, i.e. plasma sonic speed in the plasma, $V_s = 3 \times 10^5$ m s^{-1}, and pellet cloud length of a few meters, then f_{AE} would be ∼8 to ∼15 kHz in the TJ-II sectors where the coils are positioned. Indeed, increased activity occurs during the pellet injection phases close to 15 kHz in the magnetic spectrographs of the H4P32 pick-up coil signals presented in figures 3(*c*) and 9(*c*). Given the winding area of H4P32, 0.014 m^2, and its proximity to the plasma column, the coil should be sensitive to $\delta B/B \geqslant \sim 10^{-5}$ at ∼10 kHz. Whilst it is considered tentatively that these coils could detect Alfvén emissions at ∼10 kHz, the short time needed for complete plasmoid homogenization, i.e. $\leqslant \sim 50\ \mu$s, might limit detection to plasmoids which detach near the end of a pellet lifetime. Hence, the source of the activity around 15 kHz during pellet injection in figures 3(*c*) and 9(*c*) remains uncertain at present.

4.4. Pellet impact on NBI-driven Alfvén eigenmodes

Finally, to complete this work it is convenient to outline how pellet injections impact on AEs that are driven by NBI heating in the TJ-II. In previous works, various high frequency modes (f = 150 to 300 kHz) were identified in this device for different magnetic configurations [36, 52, 53]. Given the mode frequency dependence on plasma mass density, which was outlined before, it was determined that a majority of observed modes could be attributed to global- or helicity-induced AEs [52]. However, in the same paper certain modes, in the range ∼50 to 250 kHz, were found to diverge from such a $1/\sqrt{n}$ tendency. These modes exhibited a marked dependency with net plasma current, I_p and appeared to be unaffected by the evolution of the line-averaged density. In TJ-II, plasmas are typically created using ECRH. Thereafter co- or counter-injected NBI beams can be used for additional heating and fuelling and plasmas with line-averaged electron densities in the range of 1 to 5×10^{19} m^{-3} are achieved. As noted before, the through-port NBI power is about 0.5 MW per beam and acceleration voltages are $\lesssim$32 keV. As a result, $T_e(0)$'s and $T_i(0)$'s are $\lesssim$400 eV and ∼120 eV, respectively.

As noted, AEs should be readily detectable, even at low amplitudes, in magnetic spectrographs from TJ-II. Also, as indicated in subsection 4.2, Alfvén wave frequencies can be estimated from $f_{AE} = \omega_{AE}/2\pi$ where $\omega_{AE} = B_0/2qR\sqrt{(\mu_0 \Sigma_i n_i m_i)}$. Thus, when a pellet is injected into plasma exhibiting AEs, the resultant increase in plasma density should result in a reduction in f_{AE} which can be described by $f_{AEpost}/f_{AEpre} \propto 1/\sqrt{(n_{post}/n_{pre})}$. Here subscripts *pre* and *post* refer to pre- and post-injection conditions. In figure 10, a cryogenic pellet is injected into plasma heated by NBI#1 only (co-counter injector in figure 2). The observed drops in frequency for one well-developed (222.1 kHz) mode and another less-developed (132.5 kHz) one coincide with the rapid rise in plasma density. Since only line-averaged electron density is measured in TJ-II it is assumed that electron and ion densities are similar, i.e. the working gas is hydrogen and Z_{eff} is low due to lithium wall conditioning [54]. It is found for f_{AEpost} = 222.3 kHz, that f_{AEpost}/f_{AEpre} = 0.902, and for f_{AEpost} = 132.5 kHz, that f_{AEpost}/f_{AEpre} = 0.903. In comparison, $1/\sqrt{(n_{post}/n_{pre})} = 1/\sqrt{(1.48 \times 10^{19}/1.253 \times 10^{19})} = 0.92$. These results indicate that these jumps in AEs frequencies are dominated by plasma mass density changes. It is not the intention here to delve into NBI driven AEs in TJ-II, or into other aspects such as gaps, since these topics have been treated by other authors [35, 50, 51]. However, following figure 6(*a*) in reference. [35], the well-developed mode, which appears when $\tilde{n}_e = 6.5 \times 10^{18}$ m^{-3}, and the less developed-mode, which appears when $\tilde{n}_e = 1.2 \times 10^{19}$ m^{-3}, are tentatively identified as being modes with m = 8 and m = 7, respectively. From figure 7, these may be associated with the 13/8 and 11/7 rational surfaces.

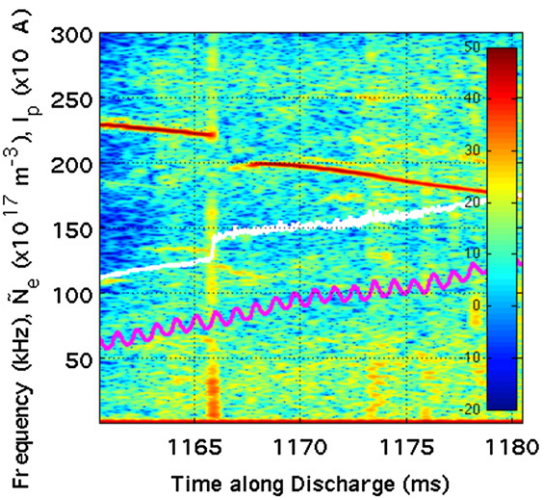

Figure 10. Magnetic spectrograph of a Mirnov coil signal (MIR5C) for discharge #44777 that was created with ECRH (1060 to 1140 ms), maintained with NBI#1 (1120 to 1220 ms), and confined using the 100_44_64 configuration. A hydrogen pellet with 5.3×10^{18} H atoms was injected at 1067 m s^{-1} into plasma having target line-averaged density = 1.23×10^{19} m^{-3}. The pellet enters the plasma at 1165.73 ms. Line-averaged electron density (white) and plasma current (magenta) are superimposed on the spectrograph.

5. Conclusions

Strengthened broadband magnetic activity is detected in magnetic coil signals during cryogenic hydrogen pellet ablation

and homogenization phases in ECRH and NBI-heated plasma in the stellarator TJ-II. This consists of a strong oscillation between ∼50 and 80 kHz which is due to interactions between outward drifting plasmoids that detach in the plasma core and a low-order rational surface near the plasma edge. Simulations obtained using a stellarator version of the HPI2 code support these arguments while analysis of signals from two newly installed toroidal arrays of magnetic pick-up coils have confirmed the identification of the low-order rational surface. In contrast, similar activity is not observed for TESPEL injections due to the significantly reduced outward drift and toroidal expansion lengths associated with TESPEL plasmoids. It is considered here that employing magnetic signals to identify low-order rational surfaces that give rise to abrupt plasmoid braking could be an important tool for understanding fuelling efficiency in stellarators. Indeed, it had been considered that plasmoid braking by low-order rational surfaces was a minor effect in stellarators but, as shown here, this may not always be the case. In this paper measurements have been limited to two TJ-II magnetic configurations having a low-order rational surface near the plasma edge. In order to achieve a better understanding of plasma conditions in which such plasmoid deceleration occurs, additional magnetic configurations, for instance, those in which the low-order rational surface being excited occurs closer to the plasma centre or those containing other low-order rational surfaces, should be studied. Indeed, the flexibility of the TJ-II makes it an ideal device for this.

The measurements presented here also reveal how broadband magnetic activity weakens significantly in TJ-II immediately after pellet ablation and homogenization. This reduction, which is strongest in ECRH plasmas, appears to be correlated with the abrupt drop in plasma electron temperature. In a previous unpublished work on TJ-II, it was observed how low-frequency density fluctuations and core electrostatic turbulence (<100 kHz) also reduce strongly for a short period after pellet injection. Again, electron temperature drop was also considered as a possible trigger mechanism. It is planned to investigate these effects in more detail in future TJ-II experimental campaigns. Finally, downward jumps in the frequencies of well-developed AEs in NBI-heated plasma are seen to arise immediately after pellet homogenization is completed. In the example presented here, the magnitude of the jump in frequency is directly related to the change in the inverse square root of the pre- and post-injection plasma mass densities.

Acknowledgments

This work has been carried out within the framework of the EUROfusion Consortium and has received funding from the Euratom research and training programme 2014–2018 and 2019–2020 under Grant Agreement No. 633053. The views and opinions expressed herein do not necessarily reflect those of the European Commission. In addition, it is partially financed by grants from the Spanish Ministerio de Ciencia e Innovación (FIS2017-89326-R and FIS2017-88892-P), by NIFS/NINS under the Project of Formation of International Scientific Base and Network (KEIN1102 and KEIN1104), by Young Researchers Supporting Program (UFEX106), and by JSPS KAKENHI (JP17KK0121 and JP19H01881). The authors thank B. Carreras for fruitful discussions.

ORCID iDs

K.J. McCarthy https://orcid.org/0000-0002-5881-1442
E. Ascasíbar https://orcid.org/0000-0001-8124-0994
N. Tamura https://orcid.org/0000-0003-1682-1519
I. García-Cortes https://orcid.org/0000-0002-5223-391X
B. van Milligen https://orcid.org/0000-0001-5344-6274
A. Cappa https://orcid.org/0000-0002-2250-9209
G. Motojima https://orcid.org/0000-0001-5522-3082
I. Pastor https://orcid.org/0000-0003-0891-0941

References

[1] Milora S.L., Houlberg W.A., Lengyel L.L. and Mertens V. 1995 *Nucl. Fusion* **35** 657
[2] Pégourié B. 2007 *Plasma Phys. Control. Fusion* **49** R87
[3] Sudo S. 1993 *J. Plasma Fusion Res.* **69** 1349
[4] Chang C.T. 1991 *Phys. Rep.* **206** 143
[5] Garnier D.T., Mauel M.E., Roberts T.M., Kesner J. and Woskov P.P. 2017 *Phys. Plasmas* **24** 012506
[6] da Cruz D.F., Chu C.C., Hogeweij G.M.D., Cardozo N.J.L., Oomens A.A.M. and Pijper F.J. 1995 *Phys. Rev. Lett.* **75** 3685
[7] Baldzuhn J., Baylor L.R. and Lyon J.F. (W7-AS team) 2004 *Fusion Sci. Technol.* **46** 348
[8] Hollmann E.M. *et al* 2017 *Nucl. Fusion* **57** 016008
[9] McCarthy K.J. *et al* (TJ-II Team LHD Experiment Group) 2019 *Plasma Phys. Control. Fusion* **61** 014013
[10] Sakamoto R. *et al* (The LHD Experimental Group) 2004 *Nucl. Fusion* **44** 624
[11] Szepesi T., Kálvin S., Kocsis G., Lang P.T. and Senichenkov I. (ASDEX Upgrade Team) 2009 *J. Nucl. Mater.* **390–391** 507
[12] Zushi H., Harada M., Osaki T., Wakatani M. and Obiki T. (Heliotron E Group) 1991 *Proc. 18th EPS Conf.* (Berlin: Germany) vol 2 (http://libero.ipp.mpg.de/libero/PDF/EPS_18_Vol2_1991.pdf)
[13] Zushi H., Mizuuchi T., Nagasaki K., Kurimoto Y., Furukawa T., Suzuki Y., Sudo S. and Wakatani M. 1993 *Proc. IAEA Technical Committee Meeting on Pellet Injection* (Naka: Japan) (https://inis.iaea.org/search/search.aspx?orig_q=RN:25020378)
[14] Bortolon A. *et al* (The DIII-D Team) 2019 *Nucl. Fusion* **59** 084003
[15] Sakakita H. 1998 *et al* Ablation characteristics on the off-axis pellet injection with/without NBI heating in the JIPP T-IIU tokamak *Int. Congress Plasma Physics. & 25th EPS Conf. Control. Fusion Plasma Physics* (Prague: Czech Republic) (http://epsppd.epfl.ch/Praha/98icpp/B139PR.PDF)
[16] Giovannozzi E. *et al* (The FTU Team) 2005 *Nucl. Fusion* **45** 399
[17] Szepesi T., Kálvin S., Kocsis G., Lackner K., Lang P.T., Maraschek M., Pokol G. and Pór G. (ASDEX Upgrade Team) 2009 *Plasma Phys. Control. Fusion* **51** 125002
[18] Rahbarnia K. *et al* (Wendelstein W7-X Team) 2021 *Plasma Phys. Control. Fusion* **63** 015005
[19] Oliver H.J.C., Sharapov S.E., Breizman B.N., Fontanilla A.K., Spong D.A. and Terranova D. (JET Contributors) 2019 *Nucl. Fusion* **59** 106031
[20] Sharapov S.E., Oliver H.J.C., Breizman B.N., Fitzgerald M. and Garzotti L. (JET contributors) 2018 *Nucl. Fusion* **58** 082008

[21] TFR Group 1987 *Nucl. Fusion* **27** 1975
[22] Kumar S.T.A. *et al* 2012 *Phys. Plasmas* **19** 056121
[23] McCarthy K.J. *et al* (The TJ-II Team) 2017 *Europhys. Lett.* **120** 25001
[24] Strauss H.R. and Park W. 1998 *Phys. Plasmas* **5** 2676
[25] Ascasíbar E. *et al* 2019 *Nucl. Fusion* **59** 112019
[26] Fernández Á., Likin K.M., Turullols P., Teniente J., Gonzalo R., del Río C., Martí-Canales J., Sorolla M. and Martín R. 2000 *Int. J. Infrared Millimeter Waves* **21** 1945
[27] Liniers M. *et al* 2013 *Fusion Eng. Des.* **88** 960
[28] McCarthy K.J. *et al* 2008 *Rev. Sci. Instrum.* **79** 10F321
[29] Combs S.K. *et al* 2013 *Fusion Sci. Technol.* **64** 513
[30] Tamura N. *et al* (TJ-II Team) 2016 *Rev. Sci. Instrum.* **87** 11D619
[31] McCarthy K.J. *et al* 2017 *Nucl. Fusion* **57** 056039
[32] Panadero N. *et al* (TJ-II Team and W7-X Team) 2018 *Nucl. Fusion* **58** 026025
[33] McCarthy K.J. 2011 Diagnostic tools for probing hot magnetically confined plasmas (https://rsef.es/images/Fisica/XXXIII_RBF_IV.pdf) *XXXIII Reunión Bienal de la Real Sociedad Española de Física: 21er Encuentro Ibérico para la Enseñanza de la Física: PUBliCan* (Santander, Spain: ediciones de la Universidad de Cantabria) IV 65
[34] Herranz J., Castejón F., Pastor I. and McCarthy K.J. 2003 *Fusion Eng. Des.* **65** 525
[35] de la Luna E. *et al* (TJ-II Team) 2001 *Fusion Eng. Des.* **53** 147
[36] Jiménez-Gómez R. *et al* 2011 *Nucl. Fusion* **51** 033001
[37] Ascasíbar E. 2021 private communication.
[38] Matsuyama A., Koechl F., Pégourié B., Sakamoto R., Motojima G. and Yamada H. 2012 *Plasma Fusion Res.* **7** 1303006
[39] Matsuyama A., Koechl F., Pégourié B., Sakamoto R., Motojima G. and Yamada H. 2012 *Nucl. Fusion* **52** 123017
[40] Rozhansky V., Senichenkov I., Veselova I. and Schneider R. 2004 *Plasma Phys. Control. Fusion* **46** 575
[41] Senichenkov I.Y., Veselova I.Y., Rozhansky V.A. and Schneider R. 2005 *J. Nucl. Mater.* **337–339** 446
[42] Pégourié B., Waller V., Nehme H., Garzotti L. and Géraud A. 2007 *Nucl. Fusion* **47** 44
[43] Köchl F., Pégourié B., Matsuyama A., Nehme H., Waller V., Frigione D., Garzotti L., Kamelander G. and Parail V. (JET EFDA Contributors) 2012 Modelling of pellet particle ablation and deposition: the hydrogen pellet injection code HPI2 (EUROfusion) Preprint EFDA-JET-PR 57 (https://scipub.euro-fusion.org/jetarchive?wpv-jet_type=preprints)
[44] Kerschen G., Golinval J.-C., Vakakis A.F. and Bergman L.A. 2005 *Nonlinear Dyn.* **41** 147
[45] van Milligen B.P., Sánchez E., Alonso A., Pedrosa M.A., Hidalgo C., de Aguilera A.M. and Fraguas A.L. 2015 *Plasma Phys. Control. Fusion* **57** 025005
[46] van Milligen B.P., García L., Carreras B.A., Pedrosa M.A., Hidalgo C., Alonso J.A., Estrada T. and Ascasíbar E. 2012 *Nucl. Fusion* **52** 013006
[47] Arévalo J., Alonso J.A., McCarthy K.J. and Velasco J.L. 2013 *Nucl. Fusion* **53** 023003
[48] Alfvén H. 1942 *Nature* **150** 405
[49] Motojima G., Sakamoto R., Goto M., Matsuyama A., Mishra J. S. and Yamada H. 2012 *Rev. Sci. Instrum.* **83** 093506
[50] Parks P.B., Sessions W.D. and Baylor L.R. 2000 *Phys. Plasmas* **7** 1968
[51] Drell S.D., Foley H.M. and Ruderman M.A. 1965 *J. Geophys. Res.* **70** 3131
[52] Sun B.J., Ochando M.A. and López-Bruna D. 2015 *Nucl. Fusion* **55** 093023
[53] Cappa Á. *et al* (TJ-II Team) 2021 *Nucl. Fusion* **61** 066019
[54] Tabarés F.L. *et al* (The TJ-II Team) 2008 *Plasma Phys. Control. Fusion* **50** 124051